symmetry

MDPI

Article

Numerical Simulations through PCM for the Dynamics of Thermal Enhancement in Ternary MHD Hybrid Nanofluid Flow over Plane Sheet, Cone, and Wedge

Muhammad Bilal [1], Ikram Ullah [2], Mohammad Mahtab Alam [3], Wajaree Weera [4,*] and Ahmed M. Galal [5,6]

1 Department of Mathematics, City University of Science and IT, Peshawar 25000, Pakistan
2 Department of Natural Sciences and Humanities, University of Engineering and Technology, Mardan 23200, Pakistan
3 Department of Basic Medical Sciences, College of Applied Medical Science, King Khalid University, Abha 61421, Saudi Arabia
4 Department of Mathematics, Faculty of Science, Khon Kaen University, Khon Kaen 40002, Thailand
5 Department of Mechanical Engineering, College of Engineering in Wadi Alddawasir, Prince Sattam Bin Abdulaziz University, Wadi Alddawasir 11991, Saudi Arabia
6 Production Engineering and Mechanical Design Department, Faculty of Engineering, Mansoura University, Mansoura P.O. Box 35516, Egypt
* Correspondence: wajawe@kku.ac.th

Abstract: The Darcy ternary hybrid nanofluid flow comprising titanium dioxide (TiO_2), cobalt ferrite ($CoFe_2O_4$) and magnesium oxide (MgO) nanoparticles (NPs) through wedge, cone, and plate surfaces is reported in the present study. TiO_2, $CoFe_2O_4$, and MgO NPs were dispersed in water to synthesize a trihybrid nanofluid. For this purpose, a mathematical model was calculated to augment the energy transport rate and efficiency for variety of commercial and medical functions. The consequences of heat source/sink, activation energy, and the magnetic field are also analyzed. Such problems mostly occur in symmetrical phenomena and are applicable to engineering, physics, and applied mathematics. The phenomena were formulated in the form of a nonlinear system of PDEs, which are simplified to the system of dimensionless ODEs through similarity replacement (obtained from symmetry analysis). The obtained set of differential equations is resolved through a parametric continuation approach (PCM). Graphical depictions are used to evaluate and address the impact of significant factors on energy, mass, and flow exchange rates. The velocity and energy propagation rates over a cone surface were greater than those of a wedge and plate versus the variation of Grashof number, porosity effect, and heat source, while the mass transfer ratio under the impact of a chemical reaction and activation energy over a wedge surface was higher than that of a plate.

Keywords: ternary hybrid nanofluid; permeable medium; cone; wedge and plate; heat source/sink; activation energy; parametric continuation method

check for updates

Citation: Bilal, M.; Ullah, I.; Alam, M.M.; Weera, W.; Galal, A.M. Numerical Simulations through PCM for the Dynamics of Thermal Enhancement in Ternary MHD Hybrid Nanofluid Flow over Plane Sheet, Cone, and Wedge. *Symmetry* **2022**, *14*, 2419. https://doi.org/10.3390/sym14112419

Academic Editors: Mikhail Sheremet and Alexey V. Lukoyanov

Received: 19 August 2022
Accepted: 2 November 2022
Published: 15 November 2022

1. Introduction

Researchers are devoting special attention to hybrid nanofluid flow across different geometries, such as a wedge, plate, and vertical cone, due to its wide range of applications in science and industry [1–3]. Rawat et al. [4] numerically examined steady micropolar fluid in the existence of a magnetic flux, mixed convection, and thermal radiation over two different configurations, cone and wedge. Gul et al. [5] documented and examined the comportment of nanofluids, and hybrid NFs allowed for moving freely on an expanding sheet. As opposed to conventional ferrofluid, the hybrid NF is more efficacious in a heat passage. Chamkha [6] addressed the mass and energy transmission properties of viscous nanofluids flowing through converging–diverging sheets with extending or decreasing walls across MHD nanoliquid flow. Bilal et al. [7] described the unsteady thermoconvective flow of nanofluid through an absorbent extended container with mass and energy conversion. Reddy and Reddy [8] investigated the nanofluid flow over the top of slice with slip conditions and chemical reactions. It is observed that as the angle of the wedge component is increased, the heat dispersion of the liquid becomes more intense in both stable and unsteady scenarios. Makinde et al. [9] studied the influence of linear heat flux, an exterior electromagnetic field, heat source, and buoyant force on the viscous fluid stream with heat allocation in three distinct topologies (cone, plate, and wedge). Relative to the two other shapes, the thermal boundary layer is more effective in flow through a wedge than that through a plate and cone. Algehyne et al. [10] reported that the nanofluid flow consists of motile microbes and nanomaterials through a permeable vertical stirring sheet. With the effects of porosity and inertial effect, the drag coefficient decreased. He and Abd et al. [11], and Marin et al. [12] numerically investigated the viscous dissipation affects over nanofluid flow across a shrinking and stretching surface. Another recent study was related to fluid flow over distinct geometries [13–20].

When compared to conventional fluids, the trihybrid nanoliquid performs well in the transition of energy conduction. Hybrid nanoliquids have an inclusive series of thermal properties and applications [21]. Hybrid nanoliquids are employed in heat exchangers, the car industry, ships, electric chillers, and broadcasters. In this study, we used a trihybrid nanofluid consisting of TiO_2, $CoFe_2O_4$ and MgO. TiO_2 is an inorganic chemical that has been utilised for over a decade in a number of applications. It is reliable because of its phosphorescence, and nontoxic and nonreactive characteristics. It is the world's brightest and frostiest substance, with reflecting properties and a UV light absorption capability that can protect from skin cancer [22–25]. MgO is a stain-resistant material that occurs naturally and serves as a magnesium source. Its overall structure comprises Mg^{2+} and O^{2-} ion connections. Bilal et al. [26] investigated the upshots of electromagnetic interaction on energy transference through water-based hybrid nanocomposites via twin turning discs. Ullah et al. [27–29] examined the influence of Darcy–Forchheimer and Coriolis force on nanofluid flow consisting of CNTs in ethylene glycol across a circling edge. Krishna et al. [30] mathematically investigated the effects of ion slip and Hall on an unstable laminar MHD convection revolving flow of second-grade fluid across a semi-infinite upward sliding porous medium. Arif et al. [31] revealed the comportment of ternary hybrid NF in Al_2O_3, Graphene and CNTs. The trihybrid nanoliquid boosted the energy transmission ratio up to 33.67%, as compared to the nano and hybrid nanoliquids. Sahoo et al. [32] used CNTs, Al_2O_3, and graphene ternary hybrid NF to reduce heat transmission in a condenser. Fattahi and Karimi [33] used a ternary hybrid nanofluid to conduct and test solar-panel efficiency with the use of the hybrid nanofluid. Some related works and uses of $CoFe_2O_4$ and Cu NPs in solvent for biological and production purposes can be found in [34–37].

Magnetisation is a crucial part of production and engineering that has a wide range of applications. The quality of heat transmission, compressors, and clutches, among other manufacturing goods, is affected by the collaboration of fluid NPs with a magnetic flux. Magnetisation can regulate the refrigeration rate in a wide range of industrial equipment. Countless academics contributed fluid mechanics research papers that explained flow properties when a magnetic field was applied. Hayat et al. [38] observed the upshot of a created magnetic field and thermal extension on the oscillating transport of nanofluid via an upright channel. The influences of the pre-exponential constituent and heat conservation in MHD mixed convection flow along an irregular surface were documented by Raju et al. [35]. Some new studies on MHD ternary and simple hybrid nanoliquid can be found in [39–42].

Following the above discussed studies, the computational modeling of Darcy–Forchheimer ternary hybrid nanofluid flow via porous wedge, cone, and plate has not yet been inspected. Therefore, our contributions are given as follows:

- To mathematically model the Darcy–Forchheimer ternary hybrid nanofluid flow via a porous wedge, cone, and plate.

- A trihybrid nanofluid is prepared by dispersing TiO_2, $CoFe_2O_4$, and MgO NPs in base liquid water.
- The Lorentz and gravitational effects are considered to see the variations in hybrid nanofluid motion.
- A mathematical model is obtained with the objective of optimizing energy transmission rates and productivity for a variety of commercial and medical applications. This research looks at the effects of heat source/sink, activation energy, and magnetic field.
- To solve the obtained system of ODEs through the PCM technique.

2. Mathematical Formulation

We assumed a steady and incompressible 2D Darcy–Forchheimer ternary hybrid nanoliquid (NF) flow over three distinct geometries (plate, wedge and cone) in the presence of a heat source/sink and activation energy. The y axis was taken to be normal to the surface, while the x axis was chosen along the surface. Figure 1 reveals the physical illustrations of the proposed problem. Further, Ω is the full angle of the wedge, γ the half-angle of the cone and r is the radius of cone. T_w and C_w are at the surface, and T_∞ and C_∞ are far away from the surface. The basic equations that operate the fluid flow were modeled as follows [43]:

$$\frac{\partial(r^{n_2}u)}{\partial x} + \frac{\partial(r^{n_2}v)}{\partial x} = 0, \tag{1}$$

$$u\frac{\partial u}{\partial x} + v\frac{\partial u}{\partial y} = \nu_{Thnf}\frac{\partial^2 u}{\partial y^2} - \nu_{Thnf}\frac{u}{K^*} + \frac{g\rho_f(T-T_\infty)\beta_T\cos\gamma}{\rho_{Thnf}} - \sigma_{Thnf}B_0^2 u - Fu^2, \tag{2}$$

$$u\frac{\partial T}{\partial x} + v\frac{\partial T}{\partial y} = \frac{k_{Thnf}}{(\rho C_p)_{Thnf}}\left(\frac{\partial^2 T}{\partial y^2}\right) + \frac{Q_0(T-T_\infty)}{(\rho C_p)_{Thnf}}, \tag{3}$$

$$u\frac{\partial C}{\partial x} + v\frac{\partial C}{\partial y} = D_B\left(\frac{\partial^2 C}{\partial y^2}\right) - k_r^2\left(\frac{T}{T_\infty}\right)^n e^{-\frac{Ea}{KT}}(C-C_\infty). \tag{4}$$

where k_r^2 is the rate of chemical reaction; Ea, Q_0, K^* and $F = C_b/rK^{*1/2}$ are the activation energy, heat source term, porosity term and nonuniform inertia term, respectively. u, v signifies the velocity along the x and y directions, respectively, β_T is the volumetric thermal expansion term, g is gravity acceleration, $(T/T_\infty)^n e^{-\frac{Ea}{KT}}$ is the modified Arrhenius constraint, and D_B is the Brownian diffusion. The slip condition was considered for the fluid velocity to be $u = U_w + L\frac{\partial u}{\partial y}$. The boundary conditions are:

$$u \to 0,\ T \to T_\infty,\ C \to C_\infty \text{ as } y \to \infty \tag{5}$$

The mathematical expression used for the ternary hybrid nanofluid flow model is expressed as follows [44,45]:

Viscosity	$\frac{\mu_{Thnf}}{\mu_f} = \frac{1}{(1-\phi_{MgO})^{2.5}(1-]\phi_{TiO_2})^{2.5}(1-\phi_{CoFe_2O_4})^{2.5}},$
Density	$\frac{\rho_{Thnf}}{\rho_f} = (1-\phi_{TiO_2})\left[(1-\phi_{TiO_2})\left\{(1-\phi_{CoFe_2O_4}) + \phi_{CoFe_2O_4}\frac{\rho_{CoFe_2O_4}}{\rho_f}\right\} + \phi_{TiO_2}\frac{\rho_{TiO_2}}{\rho_f}\right] + \phi_{MgO}\frac{\rho_{MgO}}{\rho_f},$
Specific heat	$\frac{(\rho cp)_{Thnf}}{(\rho cp)_f} = \phi_{MgO}\frac{(\rho cp)_{MgO}}{(\rho cp)_f} + (1-\phi_{MgO})\left[(1-\phi_{TiO_2})\left\{(1-\phi_{CoFe_2O_4}) + \phi_{CoFe_2O_4}\frac{(\rho cp)_{CoFe_2O_4}}{(\rho cp)_f}\right\} + \phi_{TiO_2}\frac{(\rho cp)_{TiO_2}}{(\rho cp)_f}\right]\Bigg\}$
Thermal conduction	$\left.\begin{array}{l} \frac{k_{Thnf}}{k_{hnf}} = \left(\frac{k_{CoFe_2O_4}+2k_{hnf}-2\phi_{CoFe_2O_4}(k_{hnf}-k_{CoFe_2O_4})}{k_{CoFe_2O_4}+2k_{hnf}+\phi_{CoFe_2O_4}(k_{hnf}-k_{CoFe_2O_4})}\right), \frac{k_{hnf}}{k_{nf}} = \left(\frac{k_{TiO_2}+2k_{nf}-2\phi_{TiO_2}(k_{nf}-k_{TiO_2})}{k_{TiO_2}+2k_{nf}+\phi_{TiO_2}(k_{nf}-k_{TiO_2})}\right), \\ \frac{k_{nf}}{k_f} = \left(\frac{k_{MgO}+2k_f-2\phi_{MgO}(k_f-k_{MgO})}{k_{MgO}+2k_f+\phi_{MgO}(k_f-k_{MgO})}\right), \end{array}\right\}$
Electrical conductivity	$\left.\begin{array}{l} \frac{\sigma_{Thnf}}{\sigma_{hnf}}\left(1+\frac{3\left(\frac{\sigma_{CoFe_2O_4}}{\sigma_{hnf}}-1\right)\phi_{CoFe_2O_4}}{\left(\frac{\sigma_{CoFe_2O_4}}{\sigma_{hnf}}+2\right)-\left(\frac{\sigma_{CoFe_2O_4}}{\sigma_{hnf}}-1\right)\phi_{CoFe_2O_4}}\right) \begin{array}{l} , \frac{\sigma_{hnf}}{\sigma_{nf}} = \left(1+\frac{3\left(\frac{\sigma_{TiO_2}}{\sigma_{nf}}-1\right)\phi_{TiO_2}}{\left(\frac{\sigma_{TiO_2}}{\sigma_{nf}}+2\right)-\left(\frac{\sigma_{TiO_2}}{\sigma_{nf}}-1\right)\phi_{TiO_2}}\right) \\ , \frac{\sigma_{nf}}{\sigma_f} = \left(1+\frac{3\left(\frac{\sigma_{MgO}}{\sigma_f}-1\right)\phi_{MgO}}{\left(\frac{\sigma_{MgO}}{\sigma_f}+2\right)-\left(\frac{\sigma_{MgO}}{\sigma_f}-1\right)\phi_{MgO}}\right) \end{array} \end{array}\right\}.$

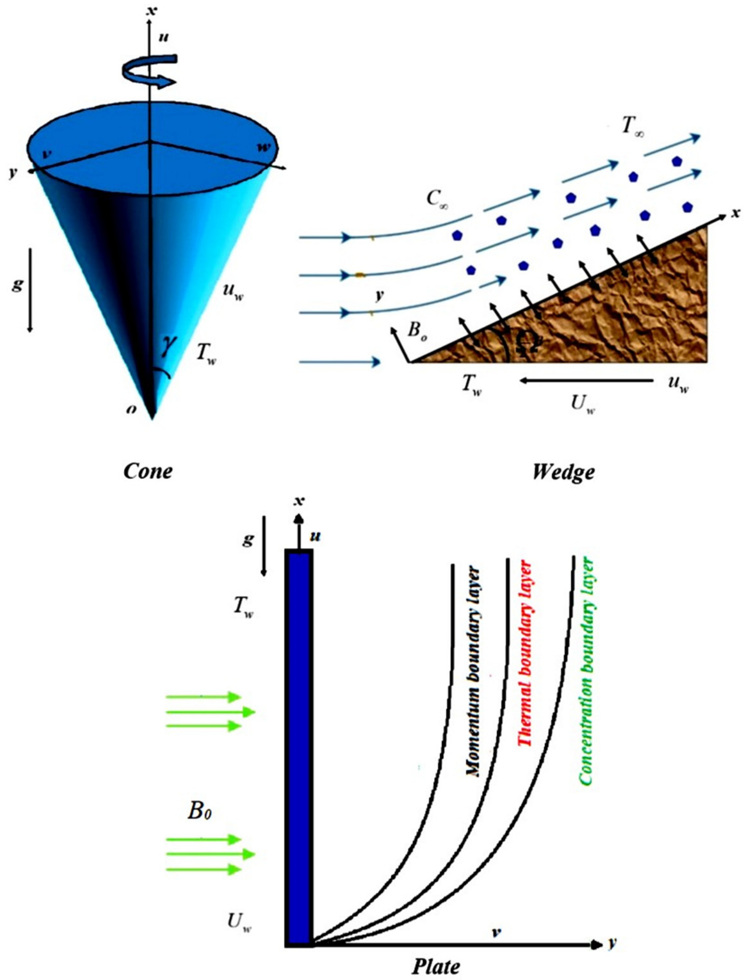

Figure 1. Ternary hybrid nanofluid flow through distinct geometries.

On the basis of above assumptions, three different geometries are described for the proposed problem as:

1. Case 1: Wedge $\rightarrow n_2 = 0$ and $\gamma \neq 0$;
2. Case 2: Cone $\rightarrow n_2 = 1$ and $\gamma \neq 0$;
3. Case 3: Plate $\rightarrow n_2 = 0$ and $\gamma = 0$.

The similarity variables are defined as:

$$\eta = \frac{y}{l},\ u = \frac{\nu_f x}{l^2} f'(\eta),\ v = \frac{-(n_2+1)}{l} f(\eta),\ \theta(\eta) = \frac{T - T_\infty}{T_w - T_\infty},\ \varphi(\eta) = \frac{C - C_\infty}{C_w - C_\infty}. \tag{6}$$

By incorporating Equation (6) into Equations (1)–(5), we obtain:

$$\left(\frac{1}{\vartheta_1 \vartheta_2}\right) f''' + f f''(n_2+1) - \left(Frf'\right)^2 + \frac{Gr\cos\gamma}{\vartheta_2} - \frac{\lambda f'}{\vartheta_1\vartheta_2} - M\vartheta_4 f' = 0, \tag{7}$$

$$\left(\frac{k_{Thnf}}{k_{hnf}}\right)\left(\frac{1}{\vartheta_3 Pr}\right)\theta'' + (n_2+1) f\theta' + \frac{Hs\theta}{\vartheta_1\vartheta_2} = 0, \tag{8}$$

$$\varphi'' + Sc(n_2+1) f\varphi' - Rc\, Sc(1+\delta\theta)^n e^{\frac{-E}{(1+\delta\theta)}}\varphi = 0. \tag{9}$$

where $\vartheta_1 = \frac{\mu_{hnf}}{\mu_f}$, $\vartheta_2 = \frac{\rho_{hnf}}{\rho_f}$, $\vartheta_3 = \frac{(\rho C_p)_{hnf}}{(\rho C_p)_f}$, $\vartheta_4 = \frac{\sigma_{hnf}}{\sigma_f}$, $\vartheta_5 = \frac{k_{hnf}}{k_f}$.

The transform conditions are:

$$\left.\begin{array}{l} f(0)=0,\, f'(0)=1+L_1 f''(0),\, \theta(0)=\varphi(0)=1\, at\, \eta=0 \\ f'(\infty)=0,\, \theta(\infty)=0,\, \varphi(\infty)=0\, as\, \eta\to\infty \end{array}\right\} \tag{10}$$

where Gr is the thermal Grashof number, E is the activation energy term, λ is the porosity term, Hs is the heat source and sink constraint, Rc is the chemical reaction term, δ is the temperature difference, Fr is the Darcy–Forchheimer term, M is the magnetic field, and L_1 is the slip parameter of velocity defined as follows:

$$\left.\begin{array}{l} Gr=\frac{g\beta(T_w-T_\infty)}{v_f u_w},\, E=\frac{Ea}{T_\infty K},\, \lambda=\frac{l^2}{K^*},\, Pr=\frac{(\rho Cp)\nu_f}{k},\, Hs=\frac{Q_1 l^2}{(\rho Cp)_f \nu_f},\, Rc=\frac{k_r^2 l^2}{\nu_f}, \\ Sc=\frac{v_f}{D_B},\, \delta=\frac{T_w-T_\infty}{T_\infty},\, Fr=\frac{C_b}{K^{*1/2}},\, M=\frac{\sigma_f B_0^2 l^2}{(\rho v)_f}. \end{array}\right\} \tag{11}$$

The skin friction, energy transmission, and mass transfer rates are:

$$C_{f^*}=\frac{\tau_w}{u_w^2\rho_f},\, Nu=\frac{lq_w}{(T_w-T_\infty)k_f},\, Sh=\frac{j_w\, l}{(C_w-C_\infty)D_B}. \tag{12}$$

where

$$\tau_w=\mu_{hnf}\left(\frac{\partial u}{\partial y}\right)_{y=0},\, q_w=-k_{hnf}\left(\frac{\partial T}{\partial y}\right)_{y=0},\, j_w=-D_B\left(\frac{\partial C}{\partial y}\right)_{y=0}. \tag{13}$$

The dimensionless form of Equation (17) is:

$$C_f=\frac{1}{x}C_{f^*}=\frac{f''(0)}{\vartheta_1},\, Nu=-\frac{k_{hnf}}{k_f}\theta'(0),\, Sh=-\varphi'(0). \tag{14}$$

4. Numerical Solution

The fundamental steps involved in the PCM solution methodology while dealing with the system of ODEs (7–9) [46,47].

Step 1: Simplifying the BVP to the 1st order

$$\hbar_1=f(\eta),\, \hbar_2=f'(\eta),\, \hbar_3=f''(\eta),\, \hbar_4(\eta)=\theta(\eta),\, \hbar_5=\theta'(\eta),\, \hbar_6=\varphi(\eta),\, \hbar_7=\varphi'(\eta). \tag{15}$$

By putting Equation (20) in Equations (12)–(14) and Equation (15), we obtain:

$$\left(\frac{1}{\vartheta_1\vartheta_2}\right)\hbar'_3+\hbar_1\hbar_3(n_2+1)-(Fr\hbar_2)^2+\frac{Gr\cos\gamma}{\vartheta_2}-\frac{\lambda\hbar_2}{\vartheta_1\vartheta_2}-M\vartheta_4\hbar_2=0, \tag{16}$$

$$\left(\frac{k_{Thnf}}{k_{hnf}}\right)\left(\frac{1}{\vartheta_3 Pr}\right)\hbar'_5+(n_2+1)\hbar_1\hbar_5+\frac{Hs\hbar_4}{\vartheta_1\vartheta_2}=0, \tag{17}$$

$$\hbar'_7+Sc(n_2+1)\hbar_1\hbar_7-Rc\, Sc(1+\delta\hbar_4)^n e^{\frac{-E}{(1+\delta\theta)}}\hbar_6=0. \tag{18}$$

The transform conditions are:

$$\left.\begin{array}{l} \hbar_1(0)=0,\, \hbar_2(0)=1,\, \hbar_4(0)=\hbar_6(0)=1\, at\, \eta=0 \\ \hbar_2(\infty)=0,\, \hbar_4(\infty)=0,\, \hbar_6(\infty)=0\, as\, \eta\to\infty \end{array}\right\} \tag{19}$$

Step 2: Introducing parameter p:

$$\left(\frac{1}{\vartheta_1\vartheta_2}\right)\hbar'_3+\hbar_1(\hbar_3-1)p(n_2+1)-(Fr\hbar_2)^2+\frac{Gr\cos\gamma}{\vartheta_2}-\frac{\lambda\hbar_2}{\vartheta_1\vartheta_2}-M\vartheta_4\hbar_2=0, \tag{20}$$

$$\left(\frac{k_{Thnf}}{k_{hnf}}\right)\left(\frac{1}{\vartheta_3 Pr}\right)\hbar'_5+(n_2+1)\hbar_1(\hbar_5-1)p+\frac{Hs\hbar_4}{\vartheta_1\vartheta_2}=0, \tag{21}$$

$$\hbar'_7 + Sc(n_2+1)\hbar_1(\hbar_7 - 1)p - Rc\,Sc(1+\delta\hbar_4)^n e^{\frac{-E}{(1+\delta\theta)}}\hbar_6 = 0. \quad (22)$$

Step 3: Applying Cauchy Principal and Discretized Equations (19)–(21):

After discretization, the obtained set of equations were computed through the MATLAB code of PCM.

5. Results and Discussion

This section reveals the physics behind each figure and table plotted in this report. The core observations are:

Velocity profile $f'(\eta)$**:**

Figures 2–6 show the velocity $f'(\eta)$ outlines versus the variations in magnetic effect M, parameter Fr, thermal Grashof number Gr, porosity term λ, and nanoparticle volume friction $\phi = (\phi_1, \phi_2, \phi_3)$, respectively. The velocity field was dramatically reduced by the effect of the magnetic field, Darcy–Forchheimer term, porosity term, and NP volume fraction, while augments with the positive variation of thermal Grashof number. Physically, the resistive force (Lorentz force) opposes the flow field which causes the decline of velocity contour. That repellant force is generated due to the effects of the magnetic flux as shown in Figure 2. Similarly, the rising values of Darcy–Forchheimer and porosity constraints enhance the surface permeability, which results in the deceleration of velocity outlines $f'(\eta)$, as displayed in Figures 3 and 4, respectively. The inclusion of ternary NPs to the base fluid magnified its viscosity and density, and created a hurdle in the flow field, as shown in Figure 5. The variation in the thermal Grashof number reduces the stretching velocity of cone, wedge, and plate, and diminishes the kinetic viscosity, which provides a suitable platform for flow field $f'(\eta)$ to move fast, as elaborated in Figure 6. Figure 7 shows the velocity outlines of ternary nanoliquid drops with the rising effect of velocity slip parameter. Figure 8 shows a relative comparison of the published literature (Rekha et al. [43]) with the present outcomes. The present results are accurate and reliable.

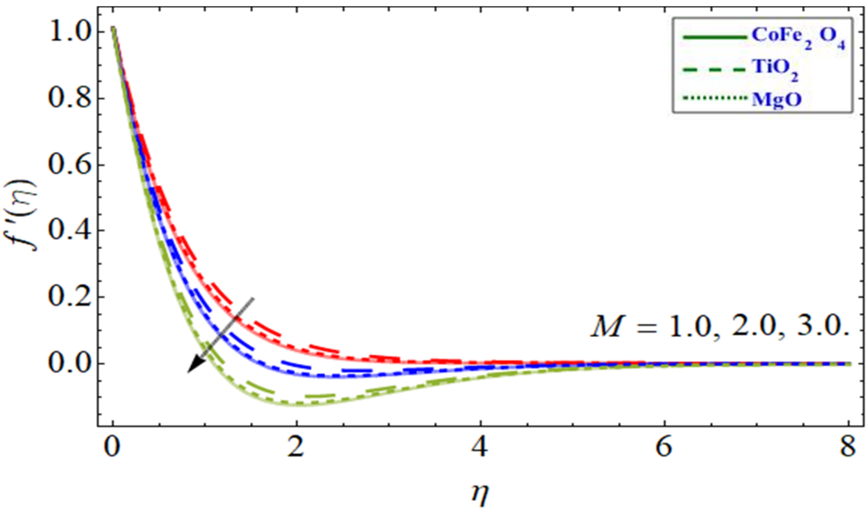

Figure 2. Magnetic parameter M effect on velocity $f'(\eta)$, where $Fr = 0.5$, $Gr = 0.1$, $\lambda = 0.5$, $M = 1.0$, $L_1 = 0$, $Hs = 0.1$, $\phi = 0.01$, $Rc = 0.4$ and $Sc = 0.1$.

Temperature $\theta(\eta)$:

Figures 9–11 show the appearance of the energy $\theta(\eta)$ profile versus the discrepancy of magnetic effect M, heat source Hs, and volume fraction of nanoparticles ϕ, respectively. Figures 9 and 10 report that the heat energy profile was boosted under the influence of the magnetic flux and heat source. As we discussed in the velocity outlines, variation in the magnetic outcome causes a resistive force that falls out in the advancement of energy profile $\theta(\eta)$. Similarly, the effect of the heat source/sink constraint also generated additional heat inside the fluid flow through all geometries (wedge, cone, and plate), which results in elevation of the temperature profile $\theta(\eta)$. Figure 11 depicts that the addition of nanoparticles to the water reduced the energy distribution. Physically, the rising quantity of the nanoparticles (TiO_2, $CoFe_2O_4$, and MgO) improved the viscosity of the trihybrid nanoliquid, which also improved the heat-absorbing capacity of the fluid; such a scenario was noticed in the energy field. Because the nanofluid absorbed more heat, the fluid temperature was kept normal. This property of the ternary nanomaterials renders them more efficient for industrial and biomedical applications. Figure 12 expresses the relative comparison of the published literature (Rekha et al. [39]) with the present outcomes for accuracy and validity purposes.

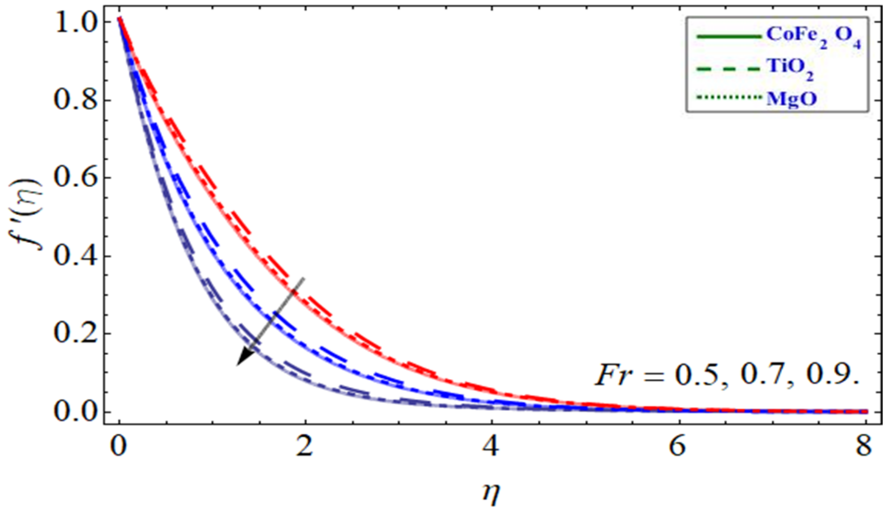

Figure 3. Darcy–Forchheimer parameter Fr effect on velocity $f'(\eta)$, where $M = 1.0$, $Gr = 0.1$, $\lambda = 0.5$, $L_1 = 0$, $M = 1.0$, $Hs = 0.1$, $\phi = 0.01$, $Rc = 0.4$ and $Sc = 0.1$.

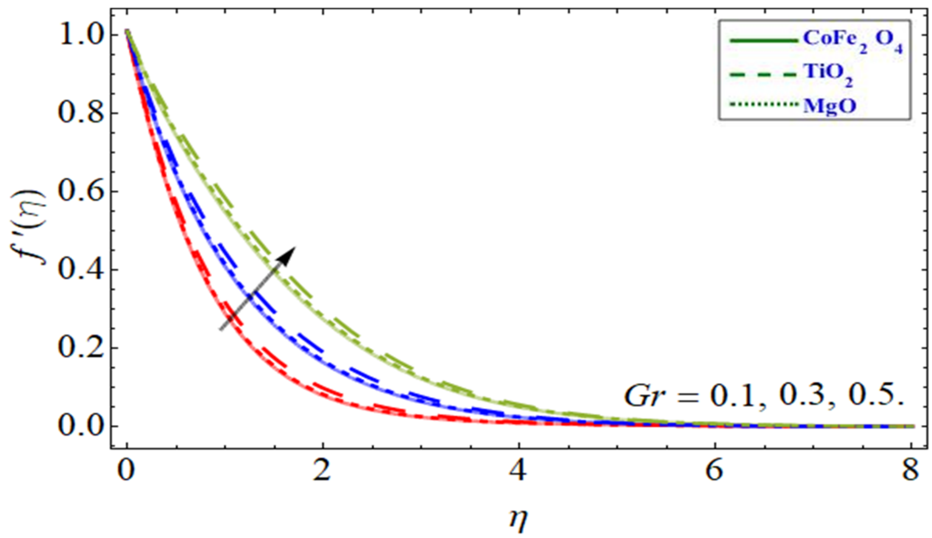

Figure 4. Thermal Grashof number Gr effect on velocity $f'(\eta)$, where $Fr = 0.5$, $M = 1.0$, $\lambda = 0.5$, $M = 1.0$, $L_1 = 0$, $Hs = 0.1$, $\phi = 0.01$, $Rc = 0.4$ and $Sc = 0.1$.

Concentration $\varphi(\eta)$:

Figures 13–15 demonstrate the mass transmission $\varphi(\eta)$ contour against the variation in chemical reaction rate Rc, Schmidt number Sc, and activation energy E, respectively. Figures 13 and 14 illustrate that the upshot of chemical reaction rate and Schmidt number reduced the mass allocation rate because the fluid kinetic viscosity was augmented with the variation in Schmidt number. This is why mass distribution $\varphi(\eta)$ decreased with this effect. The impact of the activation energy, on the other hand, boosted the mass profile, as shown in Figure 15, because activation energy term E sped up the particle kinetic energy inside the fluid, which caused the fast transfer of mass $\varphi(\eta)$ during the fluid flow.

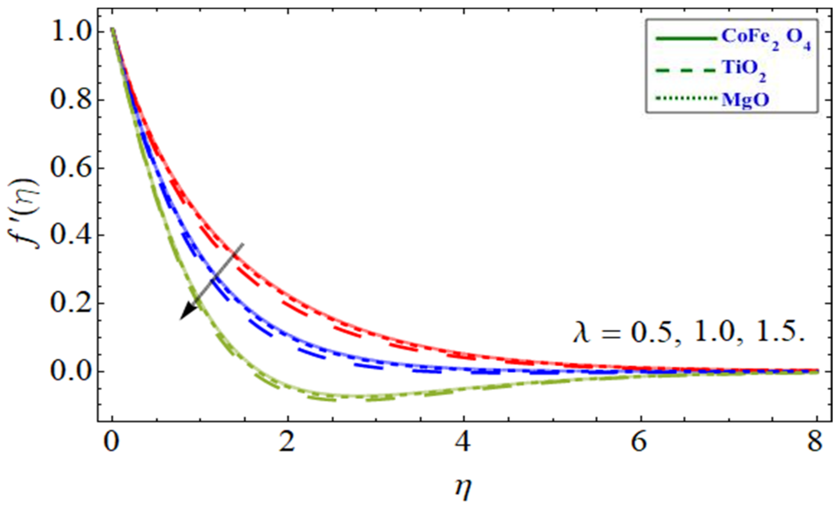

Figure 5. Porosity variable λ effect on velocity $f'(\eta)$, where $Fr = 0.5$, $M = 1.0$, $Gr = 0.1$, $M = 1.0$, $Hs = 0.1$, $\phi = 0.01$, $L_1 = 0$, $Rc = 0.4$ and $Sc = 0.1$.

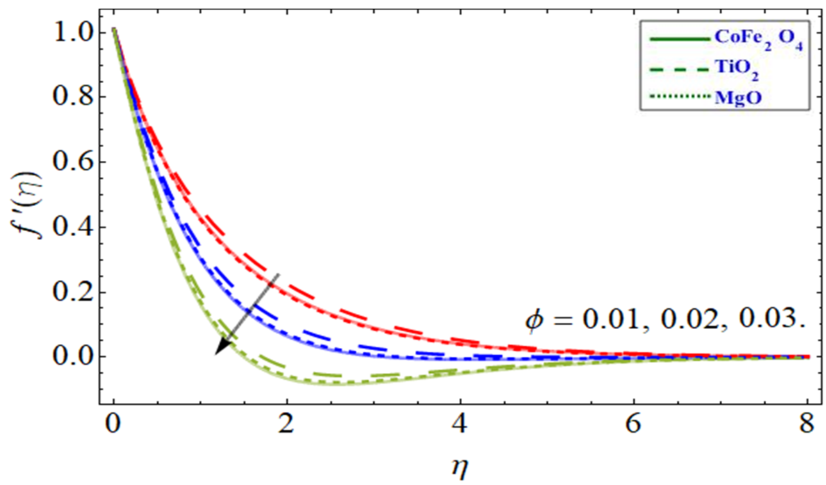

Figure 6. Nanoparticle volume friction ϕ effect on velocity $f'(\eta)$, where $Fr = 0.5$, $M = 1.0$, $Gr = 0.1$, $\lambda = 0.5$, $L_1 = 0$, $M = 1.0$, $Hs = 0.1$, $Rc = 0.4$ and $Sc = 0.1$.

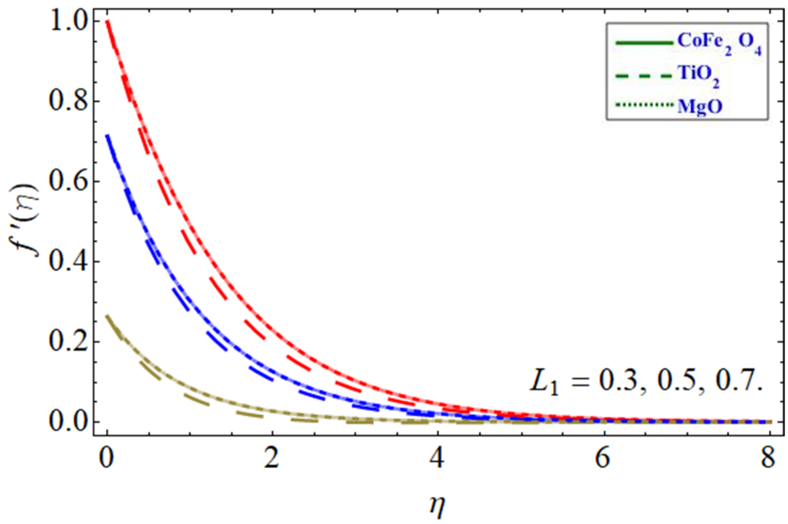

Figure 7. Velocity slip parameter L_1 effect on velocity $f'(\eta)$ profile, where $Fr = 0.5$, $M = 1.0$, $Gr = 0.1$, $\lambda = 0.5$, $M = 1.0$, $Hs = 0.1$, $Rc = 0.4$ and $Sc = 0.1$.

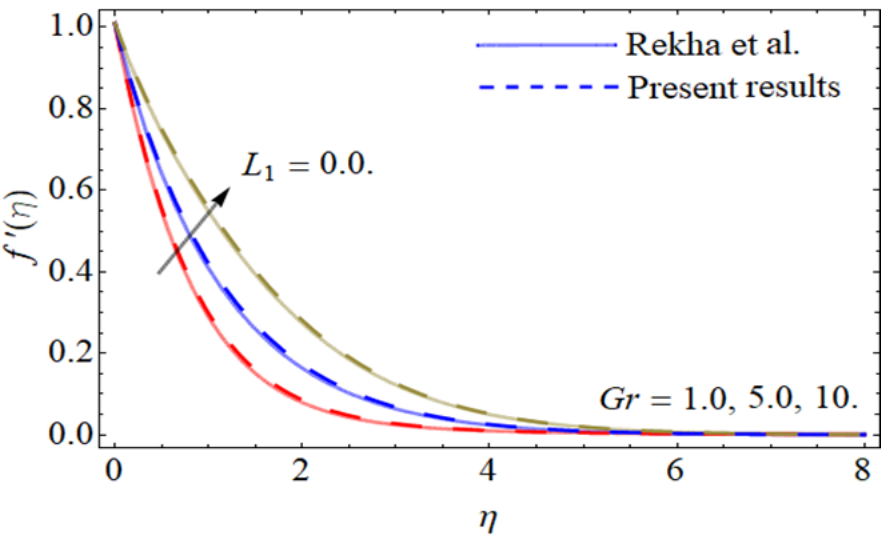

Figure 8. Comparison of published work [39] with the current results.

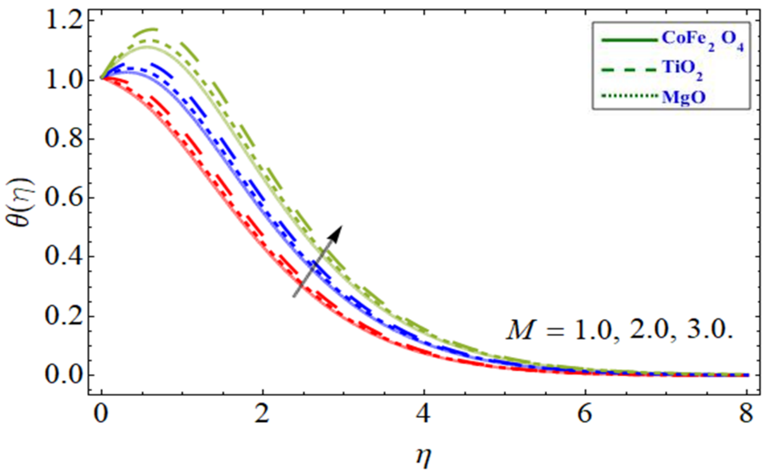

Figure 9. Magnetic term M upshot on energy contour $\theta(\eta)$, where $Fr = 0.5$, $Gr = 0.1$, $\lambda = 0.5$, $M = 1.0$, $Hs = 0.1$, $\phi = 0.01$, $Rc = 0.4$ and $Sc = 0.1$.

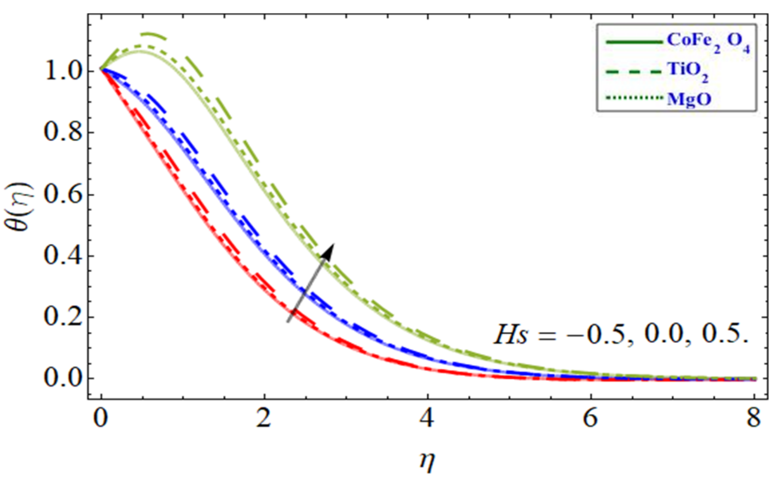

Figure 10. Heat source variable M upshot on temperature $\theta(\eta)$, where $Fr = 0.5$, $M = 1.0$, $Gr = 0.1$, $\lambda = 0.5$, $M = 1.0$, $\phi = 0.01$, $Rc = 0.4$ and $Sc = 0.1$.

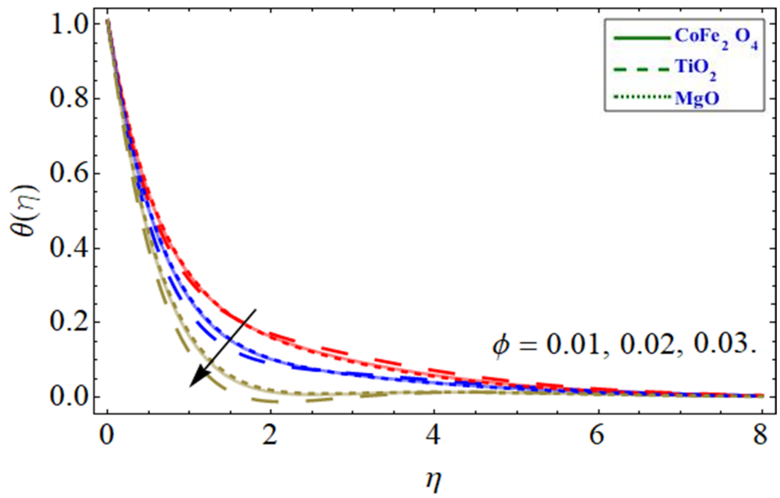

Figure 11. Volume friction of the nanoparticle ϕ effect on temperature $\theta(\eta)$, where $Fr = 0.5$, $M = 1.0$, $Gr = 0.1$, $\lambda = 0.5$, $M = 1.0$, $Hs = 0.1$, $Rc = 0.4$ and $Sc = 0.1$.

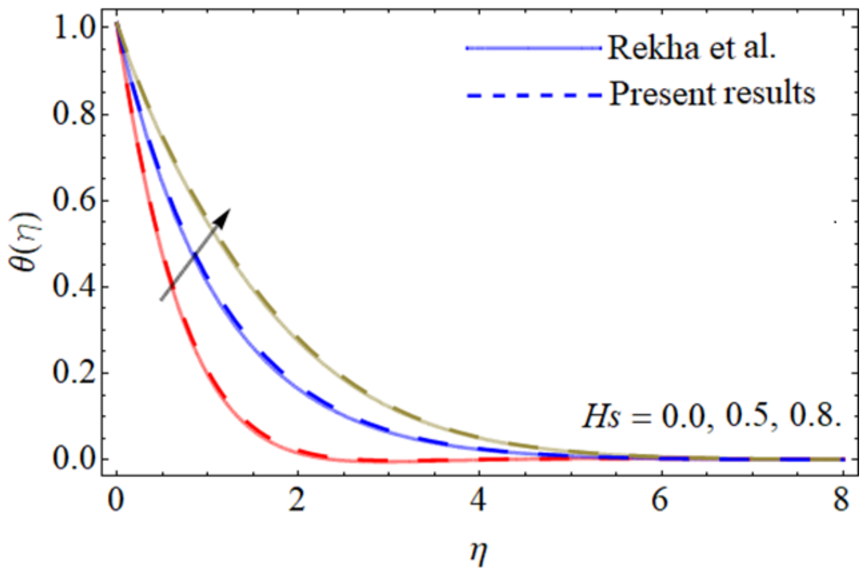

Figure 12. Comparison of published work [39] with the current results.

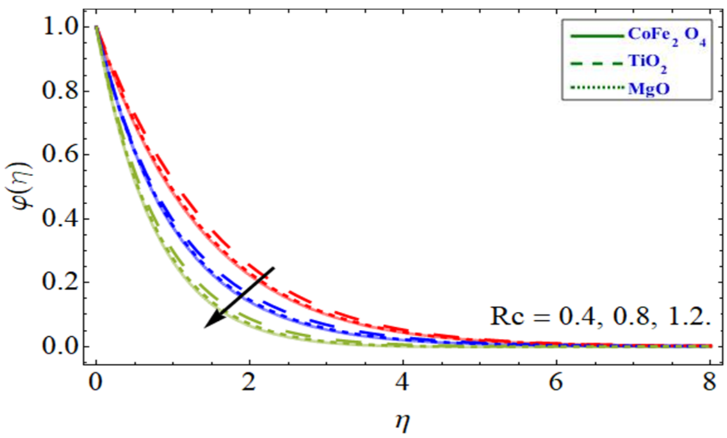

Figure 13. Chemical reaction rate Rc effect on concentration $\varphi(\eta)$, where $Fr = 0.5$, $M = 1.0$, $Gr = 0.1$, $\lambda = 0.5$, $M = 1.0$, $Hs = 0.1$, $\phi = 0.01$, and $Sc = 0.1$.

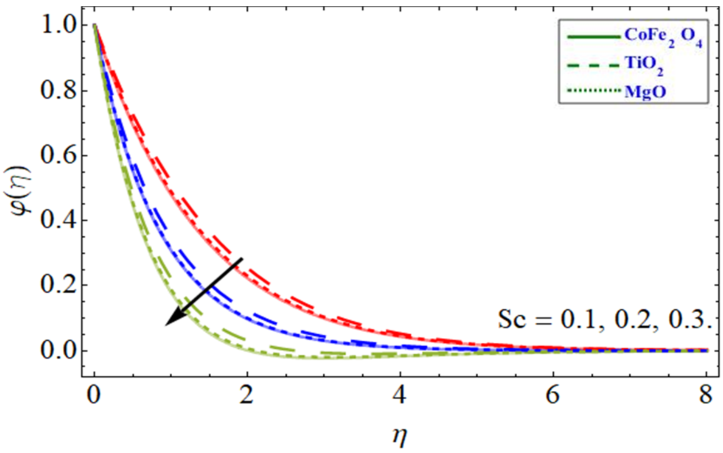

Figure 14. Schmidt number Sc effect on concentration $\varphi(\eta)$, where $Fr = 0.5$, $M = 1.0$, $Gr = 0.1$, $\lambda = 0.5$, $M = 1.0$, $Hs = 0.1$, $\phi = 0.01$, and $Rc = 0.4$.

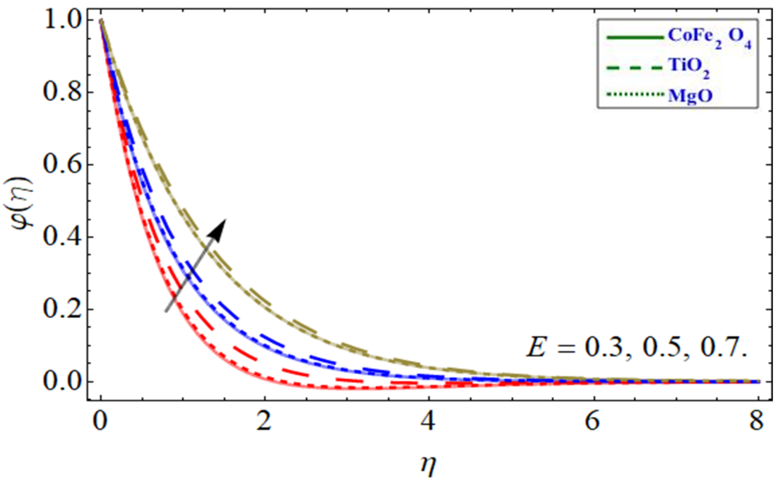

Figure 15. Activation energy parameter E effect on concentration $\varphi(\eta)$, where $Fr = 0.5$, $M = 1.0$, $Gr = 0.1$, $\lambda = 0.5$, $M = 1.0$, $Hs = 0.1$, $\phi = 0.01$, $Rc = 0.4$ and $Sc = 0.1$.

Figure 16 reveals the relative examination among the nanofluid, hybrid nanoliquid, and trihybrid nanofluid. The ternary hybrid nanoliquid flow had a clear significant impact on the energy and velocity propagation as compared to that of the nanofluid and hybrid nanofluid. Table 1 indicates the experimental values of ternary nano particulates, such as TiO_2, $CoFe_2O_4$, and MgO. Table 2 reports the arithmetic valuation of the present work with the published literature to confirm the authenticity of the current study. Tables 3 and 4 show the statistical valuations of ternary hybrid NF for skin friction $f''(0)$, energy transmission $\theta'(0)$, and mass transfer rate $\varphi'(0)$ over cone, wedge, and plate, respectively. The velocity and energy transmission over the cone were more effective than those over the wedge and plate.

Table 1. Tentative values of TiO_2, $CoFe_2O_4$, MgO NPs and water [40,41].

Base Fluid and Nanoparticles $\boldsymbol{\phi=(\phi_1=\phi_2=\phi_3)}$	ρ(**kg/m^3**)	k(**W/mK**)	Cp(**j/kgK**)	σ(**S/m**)
Pure water (H_2O)	997.1	0.613	4179	0.05
$Cobalt\ ferrite\ \phi_1 = \phi_{CoFe_2O_4}$	4907	3.7	700	5.51×10^9
$Titanium\ dioxide\ \phi_2 = \phi_{TiO_2}$	4250	8.9538	686.2	2.38×10^6
$Magnesium\ oxide\ \phi_2 = \phi_{MgO}$	3560	45	955	1.42×10^{-3}

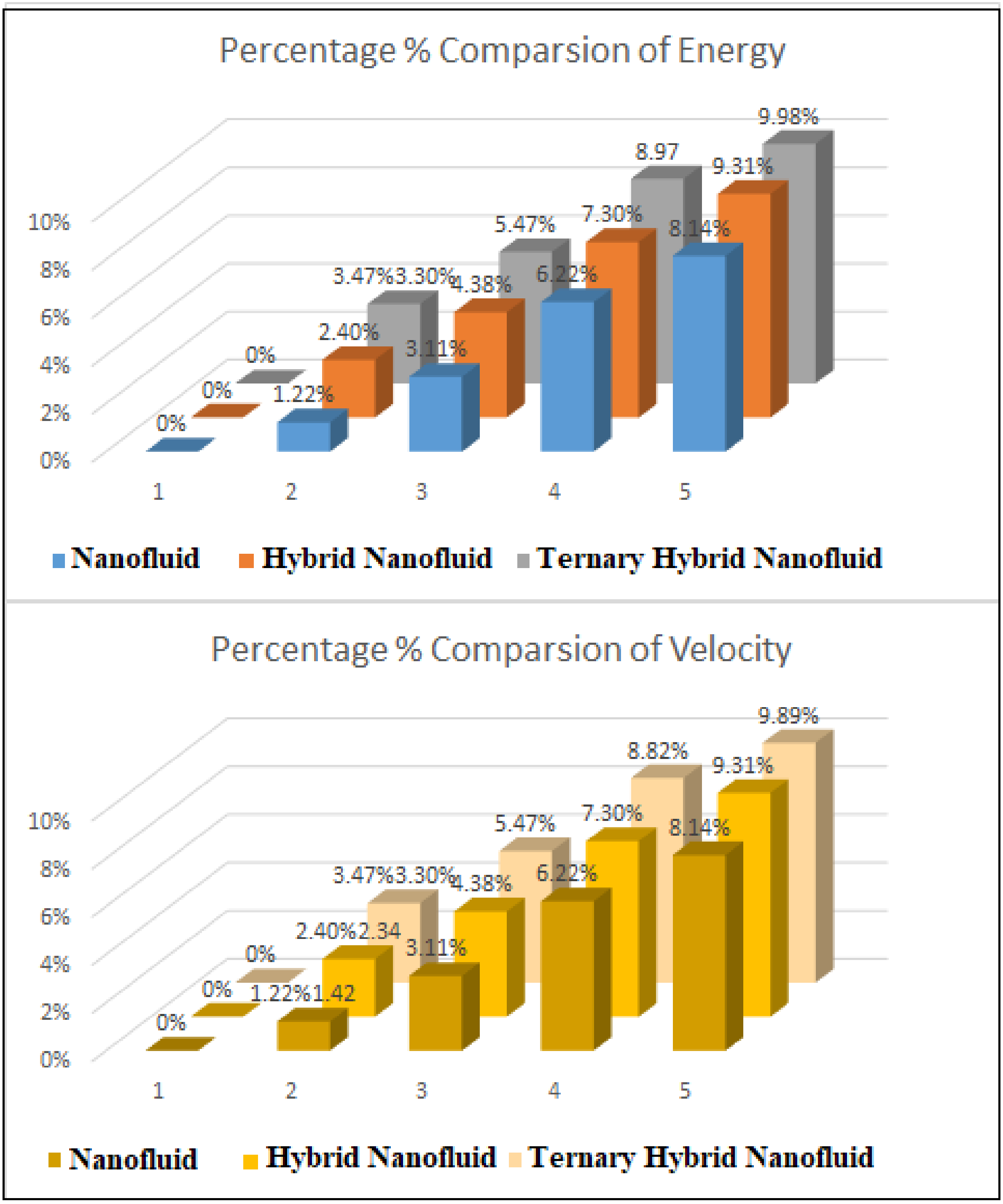

Figure 16. Comparative analysis of nanofluid, hybrid nanofluid, and ternary hybrid nanofluid.

Table 2. Statistical comparison with the existing literature for numerical outputs of $-f''(0)$.

Parameter	Kameswaran et al. [48]		Rekha et al. [39]	Present Work
λ	Analytical	Numerical	RKF-45	PCM
0.5	1.22464487	1.22464487	1.224657521	1.224758432
1.0	1.41411356	1.41411356	1.414116330	1.414217254
1.5	1.58103883	1.58103883	1.581038786	1.591139677
2.0	1.73215081	1.73215081	1.732150762	1.812052855
5.0	2.44938974	2.44938974	2.449389673	2.559489884

Table 3. Numerical outputs for $f''(0)$ and $\theta'(0)$ using numerous constraints for the cone.

Parameters			Cone		Wedge		Plate	
Gr	λ	Hs	$f''(0)$	$\theta'(0)$	$f''(0)$	$\theta'(0)$	$f''(0)$	
1.0	1.0	1.0	1.310429	1.762376	0.575218	1.183103	1.190889	1.110755
5.0			0.675524	1.832668	0.138028	1.273024	0.138028	1.273024
10			0.365352	2.104684	1.138079	1.080946	1.017223	1.401200
	1.0		1.310429	1.762376	1.301688	1.038794	1.190889	1.110755
	1.5		1.462260	1.727821	1.450276	1.199999	1.156682	1.070569
	2.0		1.602108	1.695784	1.196383	1.862916	1.307562	1.033601
		0.3	1.342571	2.321712	1.176035	1.247111	1.075516	1.872300
		0.0	1.332838	1.859068	1.133634	0.259555	1.036729	1.267148
		0.3	1.318364	1.275103	1.138079	1.080946	1.160646	0.332229

Table 4. Numerical outputs for $\varphi'(0)$ using numerous constraints for the wedge and plate.

Parameters			Wedge			Plate		
			$\varphi'(0)$			$\varphi'(0)$		
E	Rc	δ	ϕ_1=0.01 $\phi_2=\phi_3$=0	ϕ_2=0.01 $\phi_1=\phi_3$=0	ϕ_3=0.01 $\phi_1=\phi_2$=0	ϕ_1=0.01 $\phi_2=\phi_3$=0	ϕ_2=0.01 $\phi_1=\phi_3$=0	ϕ_3=0.01 $\phi_1=\phi_2$=0
0.5	0.1	0.1	0.713197	0.795709	0.563422	0.562321	0.572317	0.571158
1.0			0.632772	1.001334	0.470259	0.468917	0.480954	0.479526
1.5			0.573798	1.167276	0.400317	0.398767	0.412233	0.410574
	0.1		0.554349	0.552038	0.376497	0.374928	0.386797	0.385122
	0.3		0.692406	0.690695	0.539073	0.437966	0.547308	0.546136
	0.5		0.797092	0.795682	0.658107	0.657217	0.665194	0.864259
		0.1	0.797118	0.795709	0.658127	0.657238	0.665218	0.864283
		0.2	0.797702	0.796272	0.659114	0.658198	0.666725	0.865766
		0.3	0.798183	0.796734	0.659967	0.659027	0.668102	0.867122

3. Conclusions

The present analysis reported on the Darcy ternary hybrid nanofluid flow comprising of TiO_2, $CoFe_2O_4$, and MgO NPs through a wedge, cone, and plate. A mathematical model was created with the objective to optimize the energy and mass transfer rates, and efficiency for a variety of commercial and medical functions. The phenomena were expressed as a nonlinear system of PDEs, which were reduced to a system of dimensionless ODEs through similarity replacement. The obtained set of differential equations was solved using the PCM technique. The following are the main findings from the above assessment:

- The velocity field was dramatically reduced due to the influence of the magnetic field, the Darcy–Forchheimer term, porosity term, and NPs volume fraction, while it was augmented with the positive variation of thermal Grashof number.
- The heat energy profile was boosted under the effects of a magnetic field and heat source.
- The addition of nanoparticles (TiO_2, $CoFe_2O_4$ and MgO) to the water reduced the energy distribution.
- The mass transfer $\varphi(\eta)$ profile was reduced with the upshot of the chemical reaction rate and Schmidt number, while it was boosted with the increment of activation energy.
- The velocity and energy propagation rates over a cone surface were greater than those of the wedge and plate versus the variation in Grashof number, porosity effect, and heat source.
- The mass transfer ratio under the impact of chemical reaction and activation over a wedge surface was higher than that of a plate.
- The inclusion of ternary nanoparticles to the base fluid is significantly efficient for industrial and biomedical applications.

Author Contributions: Conceptualization, I.U.; methodology, M.B.; software, M.B.; validation, I.U.; formal analysis, M.M.A.; resources, W.W.; writing—original draft preparation, M.B. and W.W.; writing—review and editing, A.M.G.; visualization, W.W.; supervision, I.U. All authors have read and agreed to the published version of the manuscript.

Funding: This research received funding support from the NSRF via the Program Management Unit for Human Resources & Institutional Development, Research and Innovation (grant number B05F650018).

Institutional Review Board Statement: Not applicable.

Informed Consent Statement: Not applicable.

Data Availability Statement: Not applicable.

Acknowledgments: The authors would like to express their gratitude to the Research Center for Advanced Materials Science, King Khalid University, Abha, Saudi Arabia for support by grant number (RCAMS/KKU/0018-22).

Conflicts of Interest: The authors have no conflict of interest.

References

1. Li, Y.X.; Muhammad, T.; Bilal, M.; Khan, M.A.; Ahmadian, A.; Pansera, B.A. Fractional simulation for Darcy-Forchheimer hybrid nanoliquid flow with partial slip over a spinning disk. *Alex. Eng. J.* **2021**, *60*, 4787–4796. [CrossRef]
2. Marin, M.; Abbas, I.; Kumar, R. Relaxed Saint-Venant principle for thermoelastic micropolar diffusion. *Struct. Eng. Mech.* **2014**, *51*, 651–662. [CrossRef]
3. Xu, Y.J.; Bilal, M.; Al-Mdallal, Q.; Khan, M.A.; Muhammad, T. Gyrotactic micro-organism flow of Maxwell nanofluid between two parallel plates. *Sci. Rep.* **2021**, *11*, 1–13.
4. Rawat, S.K.; Upreti, H.; Kumar, M. Comparative study of mixed convective MHD Cu-water nanofluid flow over a cone and wedge using modified Buongiorno's model in presence of thermal radiation and chemical reaction via Cattaneo-Christov double diffusion model. *J. Appl. Comput. Mech.* **2020**, *7*, 1383–1402.
5. Gul, T.; Khan, A.; Bilal, M.; Alreshidi, N.A.; Mukhtar, S.; Shah, Z.; Kumam, P. Magnetic dipole impact on the hybrid nanofluid flow over an extending surface. *Sci. Rep.* **2020**, *10*, 1–13. [CrossRef]
6. Chamkha, A.J. Non-Darcy fully developed mixed convection in a porous medium channel with heat generation/absorption and hydromagnetic effects. *Numer. Heat Transf. Part A Appl.* **1997**, *32*, 653–675. [CrossRef]
7. Bilal, M.; Saeed, A.; Gul, T.; Kumam, W.; Mukhtar, S.; Kumam, P. Parametric simulation of micropolar fluid with thermal radiation across a porous stretching surface. *Sci. Rep.* **2022**, *12*, 1–11. [CrossRef]
8. Reddy, R.C.S.; Reddy, P.S. A comparative analysis of unsteady and steady Buongiorno's Williamson nanoliquid flow over a wedge with slip effects. *Chin. J. Chem. Eng.* **2020**, *28*, 1767–1777. [CrossRef]
9. Makinde, O.D.; Sandeep, N.; Animasaun, I.L.; Tshehla, M.S. Numerical exploration of Cattaneo-Christov heat flux and mass transfer in magnetohydrodynamic flow over various geometries. In *Defect and Diffusion Forum*; Trans Tech Publications Ltd.: Zürich, Switzerland, 2017; Volume 374, pp. 67–82.
10. Algehyne, E.A.; Areshi, M.; Saeed, A.; Bilal, M.; Kumam, W.; Kumam, P. Numerical simulation of bioconvective Darcy Forchhemier nanofluid flow with energy transition over a permeable vertical plate. *Sci. Rep.* **2022**, *12*, 1–12. [CrossRef]
11. He, J.H.; Abd Elazem, N.Y. Insights into partial slips and temperature jumps of a nanofluid flow over a stretched or shrinking surface. *Energies* **2021**, *14*, 6691. [CrossRef]
12. Marin, M.; Hobiny, A.; Abbas, I. The effects of fractional time derivatives in porothermoelastic materials using finite element method. *Mathematics* **2021**, *9*, 1606. [CrossRef]
13. Chamkha, A.J. Non-Darcy hydromagnetic free convection from a cone and a wedge in porous media. *Int. Commun. Heat Mass Transf.* **1996**, *23*, 875–887. [CrossRef]
14. Chamkha, A.J.; Ben-Nakhi, A. MHD mixed convection–radiation interaction along a permeable surface immersed in a porous medium in the presence of Soret and Dufour's effects. *Heat Mass Transf.* **2008**, *44*, 845–856. [CrossRef]
15. Chamkha, A.J.; Al-Mudhaf, A. Unsteady heat and mass transfer from a rotating vertical cone with a magnetic field and heat generation or absorption effects. *Int. J. Therm. Sci.* **2005**, *44*, 267–276. [CrossRef]
16. Takhar, H.S.; Chamkha, A.J.; Nath, G. MHD flow over a moving plate in a rotating fluid with magnetic field, Hall currents and free stream velocity. *Int. J. Eng. Sci.* **2002**, *40*, 1511–1527. [CrossRef]
17. Ullah, I.; Alam, M.M.; Rahman, M.M.; Pasha, A.A.; Jamshed, W.; Galal, A.M. Theoretical analysis of entropy production in exothermic/endothermic reactive magnetized nanofluid flow through curved porous space with variable permeability and porosity. *Int. Comm. Heat Mass Transfer* **2022**, *139*, 106390. [CrossRef]
18. Ullah, I.; Jan, R.U.; Khan, H.; Alam, M.M. Improving the thermal performance of (ZnO-Ni/H2O) hybrid nanofluid flow over a rotating system: The applications of Darcy Forchheimer theory. *Waves Random Complex Media* **2022**, 1–17. [CrossRef]
19. Ullah, I. Heat transfer enhancement in Marangoni convection and nonlinear radiative flow of gasoline oil conveying Boehmite alumina and aluminum alloy nanoparticles. *Int. Comm. Heat Mass Transfer* **2022**, *132*, 105920. [CrossRef]

20. Ullah, I. Activation energy with exothermic/endothermic reaction and Coriolis force effects on magnetized nanomaterials flow through Darcy–Forchheimer porous space with variable features. *Waves Random Complex Media* **2022**, 1–14. [CrossRef]
21. Waqas, H.; Imran, M.; Muhammad, T.; Sait, S.M.; Ellahi, R. Numerical investigation on bioconvection flow of Oldroyd-B nanofluid with nonlinear thermal radiation and motile microorganisms over rotating disk. *J. Therm. Anal. Calorim.* **2021**, *145*, 523–539. [CrossRef]
22. Rodríguez-González, V.; Terashima, C.; Fujishima, A. Applications of photocatalytic titanium dioxide-based nanomaterials in sustainable agriculture. *J. Photochem. Photobiol. C Photochem. Rev.* **2019**, *40*, 49–67. [CrossRef]
23. Ikram, M.D.; Imran, M.A.; Chu, Y.M.; Akgül, A. MHD flow of a Newtonian fluid in symmetric channel with ABC fractional model containing hybrid nanoparticles. *Comb. Chem. High Throughput Screen.* **2021**, *25*, 1087–1102. [CrossRef] [PubMed]
24. Munjal, S.; Khare, N.; Nehate, C.; Koul, V. Water dispersible CoFe2O4 nanoparticles with improved colloidal stability for biomedical applications. *J. Magn. Magn. Mater.* **2016**, *404*, 166–169. [CrossRef]
25. Ahmadian, A.; Bilal, M.; Khan, M.A.; Asjad, M.I. Numerical analysis of thermal conductive hybrid nanofluid flow over the surface of a wavy spinning disk. *Sci. Rep.* **2020**, *10*, 1–13. [CrossRef] [PubMed]
26. Bilal, M.; Gul, T.; Alsubie, A.; Ali, I. Axisymmetric hybrid nanofluid flow with heat and mass transfer amongst the two gyrating plates. *J. Appl. Math. Mech.* **2021**, *101*, e202000146. [CrossRef]
27. Ullah, I.; Hayat, T.; Aziz, A.; Alsaedi, A. Significance of entropy generation and the coriolis force on the three-dimensional non-darcy flow of ethylene-glycol conveying carbon nanotubes (SWCNTs and MWCNTs). *J. Non Equilib. Thermodyn.* **2022**, *47*, 61–75. [CrossRef]
28. Ullah, I.; Ali, R.; Nawab, H.; Uddin, I.; Muhammad, T.; Khan, I.; Nisar, K.S. Theoretical analysis of activation energy effect on Prandtl–Eyring nanoliquid flow subject to melting condition. *J. Non Equilib. Thermodyn.* **2022**, *47*, 1–12. [CrossRef]
29. Ullah, Z.; Ullah, I.; Zaman, G.; Khan, H.; Muhammad, T. Mathematical modeling and thermodynamics of Prandtl–Eyring fluid with radiation effect: A numerical approach. *Sci. Rep.* **2021**, *11*, 1–11. [CrossRef]
30. Krishna, M.V.; Ahamad, N.A.; Chamkha, A.J. Hall and ion slip impacts on unsteady MHD convective rotating flow of heat generating/absorbing second grade fluid. *Alex. Eng. J.* **2021**, *60*, 845–858. [CrossRef]
31. Arif, M.; Kumam, P.; Kumam, W.; Mostafa, Z. Heat transfer analysis of radiator using different shaped nanoparticles water-based ternary hybrid nanofluids with applications: A fractional model. *Case Stud. Therm. Eng.* **2020**, *31*, 101837. [CrossRef]
32. Sahoo, R.R. Heat transfer and second law characteristics of radiator with dissimilar shape nanoparticle-based ternary hybrid nanofluid. *J. Therm. Anal. Calorim.* **2021**, *146*, 827–839. [CrossRef]
33. Fattahi, A.; Karimi, N. Numerical simulation of the effects of superhydrophobic coating in an oval cross-sectional solar collector with a wavy absorber filled with water-based Al_2O_3-ZnO-Fe_3O_4 ternary hybrid nanofluid. *Sustain. Energy Technol. Assess.* **2020**, *50*, 101881. [CrossRef]
34. Ghalambaz, M.; Behseresht, A.; Behseresht, J.; Chamkha, A. Effects of nanoparticles diameter and concentration on natural convection of the Al_2O_3–water nanofluids considering variable thermal conductivity around a vertical cone in porous media. *Adv. Powder Technol.* **2015**, *26*, 224–235. [CrossRef]
35. Chamkha, A.J.; Dogonchi, A.S.; Ganji, D.D. Magneto-hydrodynamic flow and heat transfer of a hybrid nanofluid in a rotating system among two surfaces in the presence of thermal radiation and Joule heating. *AIP Adv.* **2019**, *9*, 025103. [CrossRef]
36. Ramesh, G.K.; Shehzad, S.A.; Rauf, A.; Chamkha, A.J. Heat transport analysis of aluminum alloy and magnetite graphene oxide through permeable cylinder with heat source/sink. *Phys. Scr.* **2020**, *95*, 095203. [CrossRef]
37. Ali, S.; Razzaq, A.; Kim, H.; In, S.I. Activity, selectivity, and stability of earth-abundant $CuO/Cu_2O/Cu^0$-based photocatalysts toward CO_2 reduction. *Chem. Eng. J.* **2020**, *429*, 131579. [CrossRef]
38. Hayat, T.; Noreen, S. Peristaltic transport of fourth grade fluid with heat transfer and induced magnetic field. *Comptes Rendus Mécanique* **2010**, *338*, 518–528. [CrossRef]
39. Raju, M.C.; Varma, S.V.K.; Seshaiah, B. Heat transfer effects on a viscous dissipative fluid flow past a vertical plate in the presence of induced magnetic field. *Ain Shams Eng. J.* **2015**, *6*, 333–339. [CrossRef]
40. Krishna, M.V.; Ahamad, N.A.; Chamkha, A.J. Hall and ion slip effects on unsteady MHD free convective rotating flow through a saturated porous medium over an exponential accelerated plate. *Alex. Eng. J.* **2020**, *59*, 565–577. [CrossRef]
41. VeeraKrishna, M.; Subba Reddy, G.; Chamkha, A.J. Hall effects on unsteady MHD oscillatory free convective flow of second grade fluid through porous medium between two vertical plates. *Phys. Fluids* **2018**, *30*, 023106. [CrossRef]
42. Krishna, M.V.; Chamkha, A.J. Hall and ion slip effects on MHD rotating flow of elastico-viscous fluid through porous medium. *Int. Commun. Heat Mass Transf.* **2020**, *113*, 104494. [CrossRef]
43. Rekha, M.B.; Sarris, I.E.; Madhukesh, J.K.; Raghunatha, K.R.; Prasannakumara, B.C. Activation Energy Impact on Flow of AA7072-AA7075/Water-Based Hybrid Nanofluid through a Cone, Wedge and Plate. *Micromachines* **2022**, *13*, 302. [CrossRef] [PubMed]
44. Wang, F.; Nazir, U.; Sohail, M.; El-Zahar, E.R.; Park, C.; Thounthong, P. A Galerkin strategy for tri-hybridized mixture in ethylene glycol comprising variable diffusion and thermal conductivity using non-Fourier's theory. *Nanotechnol. Rev.* **2022**, *11*, 834–845. [CrossRef]
45. Acharya, N.; Maity, S.; Kundu, P.K. Framing the hydrothermal features of magnetized TiO2–CoFe2O4 water-based steady hybrid nanofluid flow over a radiative revolving disk. *Multidiscip. Model. Mater. Struct.* **2019**. [CrossRef]

46. Shuaib, M.; Shah, R.A.; Durrani, I.; Bilal, M. Electrokinetic viscous rotating disk flow of Poisson-Nernst-Planck equation for ion transport. *J. Mol. Liq.* **2020**, *313*, 113412. [CrossRef]
47. Shuaib, M.; Shah, R.A.; Bilal, M. Von-Karman rotating flow in variable magnetic field with variable physical properties. *Adv. Mech. Eng.* **2021**, *13*, 1687814021990463. [CrossRef]
48. Kameswaran, K.; Shaw, S.; Sibanda, P.; Murthy, P. Homogeneous-heterogeneous reactions in a nanofluid flow due to a porous stretching sheet. *Int. J. Heat Mass Transf.* **2013**, *57*, 465–472. [CrossRef]